Eur. Phys. J. B **18**, 207–214 (2000)

THE EUROPEAN
PHYSICAL JOURNAL B
EDP Sciences

First principles study of electronic structure and optical properties of $CaTiO_3$

S. Saha[1], T.P. Sinha[1,a], and A. Mookerjee[2]

[1] Department of Physics, Bose Institute, 93/1 Acharya Prafulla Chandra Road, Calcutta 700009, India
[2] SN Bose National Centre for Basic Sciences, JD Block, Sector 3, Salt Lake City, Calcutta 700091, India

Received 1 February 2000 and Received in final form 21 July 2000

Abstract. The electronic-energy band structure, site and angular momentum decomposed density of states (DOS) and charge-density contours of perovskite $CaTiO_3$ are calculated by the first principles tight-binding linear muffin-tin orbitals method with atomic sphere approximation using density functional theory in its local density approximation. The calculated band structure shows an indirect (R-Γ) band gap of 1.5 eV. The total DOS as well as the partial density of states (PDOS) are compared with the experimental photoemission spectra. The calculated DOS are in reasonable agreement with the experimental energy spectra and the features in the spectra are interpreted by a comparison of the spectra with the PDOS. The origin of the various experimentally observed bands have been explained. From the DOS analysis, as well as charge-density studies, we conclude that the bonding between Ca and TiO_3 is mainly ionic and that the TiO_3 entities bond covalently. Using the projected DOS and band structure we have analyzed the interband contribution to the optical properties of $CaTiO_3$. The real and imaginary parts of the dielectric function and hence the optical constants such as refractive index and extinction coefficient are calculated. The calculated spectra are compared with the experimental results for $CaTiO_3$ and are found to be in good agreement with the experimental results. The effective number of electrons per unit cell participating in the interband transitions are calculated. The role of band structure calculation as regards the optical properties of $CaTiO_3$ is discussed.

PACS. 71.15.Mb Density functional theory, local density approximation – 78.20.Ci Optical constants (including refractive index, complex dielectric constant, absorption, reflection and transmission coefficients, emissivity) – 77.84.Dy Niobates, titanates, tantalates, PZT ceramics, etc.

1 Introduction

Ferroelectric and related perovskites having chemical formula ABO_3 are the subject of extensive investigation, both because of their technical importance and because of the fundamental interest in the physics of their phase transitions [1]. Within this family of materials, one finds transitions to a wide variety of low symmetry phases, ranging from nonpolar antiferrodistortive (AFD) to polar ferroelectric (FE) and antiferroelectric (AFE) transitions. The ideal structure is cubic perovskite, where the A and B cations are arranged on a simple cubic lattice and the O ions lie on the face centres nearest the (typically transition metal) B cations. Thus the B cations are at the centre of O octahedra, while the A cations lie at larger twelvefold-coordinated sites. This ideal structure displays a wide variety of structural instabilities in the various materials. These may involve rotations and distortions of the O octahedra as well as displacements of the cations from their ideal sites. The interplay of these instabilities accounts for the rich variety of FE and AFE behaviours. The two common instabilities result from softening of either a polar zone-centre phonon mode, leading to a FE phase, or the softening of a non-polar zone-boundary mode involving rotations of oxygen octahedra, leading to a AFD phase. In some cases a zone-boundary polar mode may also occur, leading to an AFE phase.

$CaTiO_3$ is one of the alkaline earth titanates like $BaTiO_3$ and $SrTiO_3$. These titanates have recently attracted the attention of many researchers because some titanates are practically used as ferroelectric, electroconductive, photorefractive and photovoltaic materials. It is well known that these applications are based on electrical and optical properties of the materials, and the properties result from their electronic structures. Therefore, an understanding of the electronic structure of the materials is fairly important to improve the electrical or optical functions for their new applications. $BaTiO_3$ undergoes three temperature phase transitions from a paraelectric cubic phase, stable at high temperature, to FE phases of tetragonal, orthorhombic and rhombohedral symmetry [1]. $SrTiO_3$ has the simple cubic perovskite structure

---

[a] e-mail: `tpsinha@boseinst.ernet.in`

at high temperature and goes through an AFD transition at 105 K to a tetragonal phase in which the oxygen octahedra have rotated in opposite senses in neighbouring unit cells [1]. The observed softening of the FE polar phonons with further reduction of temperature in the range 50-100 K would appear to extrapolate to a FE transition close to 20 K, but instead the softening saturates and no such transition is observed [2]. The absence of a true FE transition is suggested to be suppressed by quantum fluctuations, giving rise to a ‘quantum paraelectric’ phase at very low temperatures [3]. $CaTiO_3$ transforms from orthorhombic (Pbnm) to orthorhombic (Cmcm) followed by tetragonal (I4/mcm) and cubic ($Pm\bar{3}m$) structures with the rise of temperature from 295 to 1600 K [4]. However, there exists a controversy regarding the cubic symmetry of $CaTiO_3$ at high temperatures. Sasaki *et al.* have reported that the crystal structure of $CaTiO_3$ is distorted from the ideal cubic perovskite structure at high temperatures [5]. Buttner and Maslen [6] have also confirmed the results of Sasaki *et al.* regarding the distorted cubic perovskite structure for $CaTiO_3$ at high temperatures. But recent neutron diffraction study by Kennedy *et al.* [4] has established that above 1580 K the tilting of oxygen octahedra disappears and $CaTiO_3$ has the ideal cubic perovskite structure with space group $Pm\bar{3}m$.

The first principles theoretical studies of electronic structure and the origin of ferroelectricity in $BaTiO_3$ has started in 1985 and are performed using the linearized-muffin-tin orbital (LMTO) method [7,8]. Since then a number of workers have studied the various properties of $BaTiO_3$ and $SrTiO_3$ using first principles calculations [9 – 35]. Cohen and Krakauer [9] used the all-electron full-potential linearized augmented-plane-wave (FLAPW) method to study ferroelectricity in $BaTiO_3$ within the local density approximation (LDA). They performed a series of frozen phonon calculations and demonstrated that the phase with full cubic symmetry is unstable with respect to zone-centre distortions, in accord with the experimentally observed FE transition in this material. Later they extended this approach to the case of $PbTiO_3$ [10]. Cohen emphasized that the hybridization between the Ti 3*d* and O 2*p* is necessary for ferroelectricity in $BaTiO_3$ and $PbTiO_3$ [11]. Singh and Boyer have also used the FLAPW method to investigate ferroelectricity in $KNbO_3$ [12]. King-Smith and Vanderbilt [13,14] performed a systematic study of structural and dynamical properties and energy surfaces for eight common perovskites including $CaTiO_3$ using the first principles ultrasoft pseudopotential method and the LDA. These calculations demonstrate that ferroelectricity in the perovskites reflects a delicate balance between long-range electrostatic forces which favour the FE state and short-range repulsions which favour the cubic phase. While constrained to calculations of zero-temperature properties, these calculations yield correct predictions of ground state structures and the occurrence of FE phases for certain materials. They have shown that high-quality LDA calculations can provide considerable insight into the nature of the total-energy surface in the perovskites. For further insight into the energetics of FE compounds, the polarization generated by various distortions can be studied directly using the first principles method of King-Smith and Vanderbilt [15,16]. This approach has been applied to investigate the zone-centre phonons in the common cubic perovskite oxides [17] by performing first principles calculations of Born effective charges. Ghosez *et al.* have determined the phonon frequencies at the Γ-point from Born effective charges and dielectric tensor for the cubic and rhombohedral phases of $BaTiO_3$ using first principles calculations [18,19]. The calculations were performed within the density functional theory (DFT) and the LDA using a conjugate-gradient plane-wave pseudopotential method [20–22]. The first principles calculation of Γ phonons in $KNbO_3$ which has the same crystal structure and exhibits the same sequence of ferroelectric transitions as $BaTiO_3$, have been done by Postnikov *et al.* using the full-potential linear muffin-tin orbital (FP-LMTO) method [23,24] in the LDA. A complete first principles study of the FE phase transition in $BaTiO_3$ has been carried out by Zhong *et al.* [25,26] using Vanderbilt ultrasoft pseudopotential calculations [27] within LDA and Monte Carlo simulations. The first principles study of the finite temperature properties of eight perovskite compounds ($BaTiO_3$, $KNbO_3$, $BaZrO_3$, $PbTiO_3$, $SrTiO_3$, $NaNbO_3$, $PbZrO_3$ and $CaTiO_3$) with both FE and AFD type instabilities have been performed by Zhong and Vanderbilt [28]. They have shown that AFD instabilities are almost as common as FE ones in cubic perovskite compounds and the anharmonic on-site coupling between order parameters causes the AFD and FE instabilities to tend to suppress one another. Using Monte Carlo simulations and an *ab initio* Hamiltonian, the effects of quantum fluctuations on structural phase transitions in the cubic perovskite compounds $SrTiO_3$ and $BaTiO_3$ have been studied by Zhong and Vanderbilt [29]. They have shown that the quantum fluctuations suppress the FE transition completely and reduce the AFD transition temperature from 130 to 110 K for $SrTiO_3$. For $BaTiO_3$, quantum fluctuations do not effect the order of the transition, but do reduce the transition temperature by 35–50 K. The 180° domain walls study in tetragonal $BaTiO_3$ has been performed by Padilla *et al.* [30] using first principles ultrasoft pseudopotential calculations and Monte Carlo simulations. Using the LDA and ultrasoft pseudopotentials with a plane wave basis, Garcia *et al.* [31] have performed a first principles study of the vibrational modes of $PbTiO_3$ in the FE tetragonal phase at all the symmetry points of the Brillouin zone. Recently, the first principles total-energy calculations for the surfaces of $BaTiO_3$ [32,33] and $SrTiO_3$ [34,35] have also been performed. In contrast to these titanates, the electronic structure of $CaTiO_3$ has not been studied in detail, although it is one of the alkaline earth titanates with perovskite structure. This is probably because $CaTiO_3$ has not been widely used as a practical material, compared with $SrTiO_3$ and $BaTiO_3$. However, an understanding of the electronic structures through a series of alkaline earth titanates is significant, from the viewpoint of material science, to pursue the origins of their electrical and optical functions. The first principles investigations of some of the properties of $CaTiO_3$ (such as AFD instability, spontaneous polarization, zone-centre phonon frequency and elastic constants calculations) have been performed by Vanderbilt and co-workers [14,17,28] considering its structure as ideal cubic perovskite. Though, the electrical and optical [36–40] properties of $SrTiO_3$ and $BaTiO_3$ have been extensively examined and their electronic structures are well understood, no attempt has been made to study the optical properties of $CaTiO_3$ using the self-consistent first principles electronic band structure calculation.

Ueda *et al.* [41] have measured the vacuum ultraviolet reflectance and electron energy loss spectra of $CaTiO_3$ and evaluated the dielectric functions and optical constants using Kramers-Krönig relations. They have also measured the electronic structure of $CaTiO_3$ by X-ray and ultraviolet photoemission spectroscopy [42]. To explain the observed results theoretically, they have used the non-self-consistent linear combination of atomic orbitals (LCAO) tight-binding method [41,42]. In their non-self-consistent method, they have not considered the electron-electron Coulomb repulsion and also not been able to explain the origin of the higher energy band [42]. Hence a fresh investigation of the observed data is needed. In the present study, the electronic structure and optical properties of cubic perovskite $CaTiO_3$ are calculated by the first principles tight binding linearized muffin-tin orbital (TB-LMTO) method [43] with atomic sphere approximation (ASA) [code LMTO-47, 1995] using DFT in its LDA [44]. The first principles TB-LMTO-ASA study of the electronic structure and optical properties for $SrTiO_3$ and $BaTiO_3$ are reported elsewhere [45,46]. The first principles density-functional calculations offer an attractive approach for enhancing our microscopic understanding of perovskites. In the coming sections, the computational details regarding the methods used in our calculations of the electronic structure and optical properties are described. Finally, the calculated results are compared with the observed experimental data [41,42].

2 Computational details

We have carried out the self consistent electronic energy band structure calculations using the TB-LMTO method within ASA for cubic perovskite $CaTiO_3$. The basis sets used here comprised augmented linear muffin-tin orbitals. The exchange-correlation potential within LDA is calculated using the parametrization scheme of von Barth and Hedin [47]. The DOS has been calculated by the method of tetrahedra [48]. The calculations have been performed considering the origin of the cell to be at the Ca site, Ti at the body-centre (0.5, 0.5, 0.5)a and the three O atoms at the three face centres (0.5, 0.5, 0.0)a, (0.0, 0.5, 0.5)a and (0.5, 0.0, 0.5)a. The lattice constant is 7.37 *a.u.*, taken from the experimental results of Kennedy *et al.* [4]. The unit cell volume was filled up to 100% by the atomic spheres keeping the atom-atom overlap $\sim$ 12% and hence no empty sphere was introduced. Within the atomic spheres the basis functions, the charge density and the potential are expanded in symmetry adopted spherical harmonics together with a radial function. Basis functions up to $\ell_{\max} = 2$ for Ca, Ti and O were used. The Ca $4s$, $3p$ and $3d$, Ti $4s$, $4p$ and $3d$ and O $2s$ and $2p$ were taken in valence states whereas O $3d$ was downfolded and do not contribute to the dimension of the Hamiltonian H and overlap O matrices, but carry charge. Brillouin zone integration was carried out by tetrahedron method using a mesh of about 500 symmetry reduced points. 13 iterations were necessary to achieve self-consistency and the eigenvalues of last two iterations differ by less than 0.01 mRyd.

The linear response of the system to an external electromagnetic field with a small wave vector is measured through the complex dielectric function $\epsilon(\omega)$. The frequencies of interest to us will be well above those of phonons, so we shall consider the electronic excitations alone. This we shall do within the random phase approximation. Local-field and lifetime effects will be neglected. Lifetime broadening will be reintroduced subsequently phenomenologically by convoluting the absorptive part of $\epsilon(\omega)$ with a Lorentzian with a full-width at half-maximum (FWHM) is 8×10^{-4} Ryd at the photon energy of 0.073 Ryd, increasing quadratically with photon energy, as suggested by Ravindran *et al.* [49]. The cubic nature of $CaTiO_3$ leads to a diagonal and isotropic dielectric tensor. The imaginary part of the dielectric function $\epsilon^{''}(\omega)$ is then given by

$$\epsilon''(\omega) = \left(\frac{Ve^2}{2\pi\hbar\ m^2\omega^2}\right) \int \mathrm{d}^3\mathbf{k} \sum_{nn'} |\langle \mathbf{k}n|\mathbf{p}|\mathbf{k}n'\rangle|^2 f(\mathbf{k}n) \times \Big(1 - f(\mathbf{k}n')\delta(E_{\mathbf{k}n} - E_{\mathbf{k}n'} - \hbar\omega\Big) \tag{1}$$

where the terms have their usual meanings [45].

The matrix element is evaluated over the atomic spheres. In addition to the life-time broadening which is introduced at this stage, an additional Gaussian broadening due to instrumental resolution of FWHM of 4×10^{-4} Ryd was also incorporated.

The real part of the dielectric function $\epsilon'(\omega)$ follows from the Kramer-Krönig relationship. The optical constants such as refractive index $n(\omega)$ and the extinction coefficient $k(\omega)$ may now be derived from this ($\epsilon' = n^2 - k^2$ and $\epsilon'' = 2nk$).

It is to be noted that for the interpretation of the optical spectra of systems, it does not seem realistic to give a single transition assignment to the peaks present in a crystal reflecting spectrum since many transitions (direct to indirect) may be found in the band structure with an energy corresponding to the peak and since states outside the lines and point of symmetry could contribute to the reflectivity. Therefore, the symmetry-allowed transition energies lead to an incomplete description of the optical spectrum. We have generated theoretical curves using the customary approximation made to interpret the optical spectra from band structure calculations, namely by considering the imaginary part $\epsilon''(\omega)$ of the optical dielectric constant ϵ as proportional to the joint density of states weighted by ω^{-2}. The theoretical results are compared with the observed experimental data [41,42].

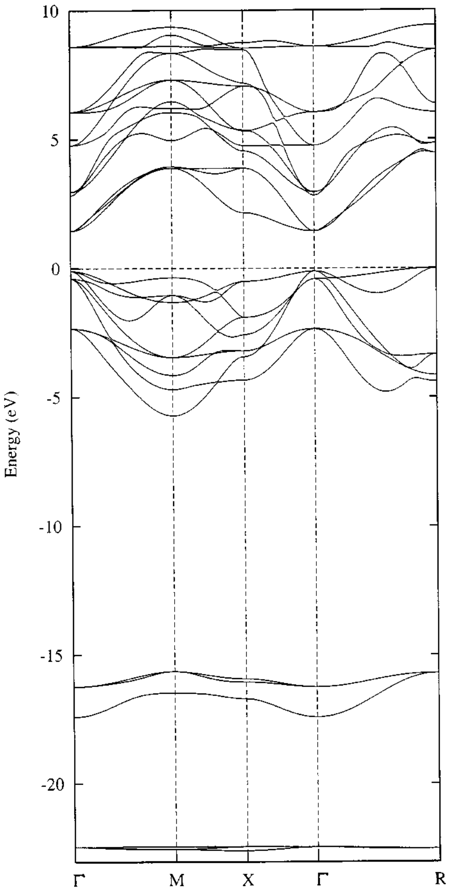

Fig. 1. The calculated electronic energy-band structure of $CaTiO_3$.

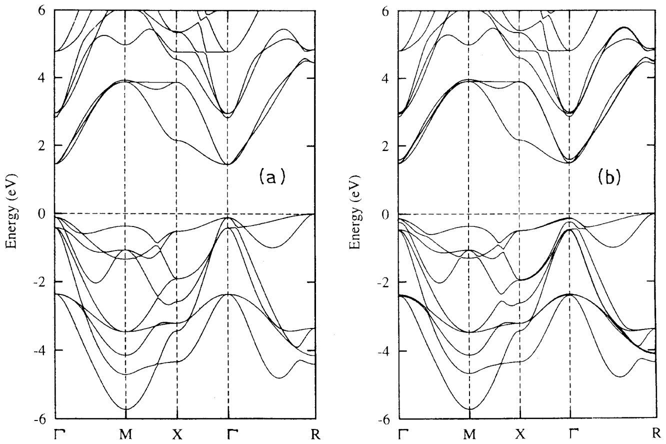

Fig. 2. A comparison of electronic band structure for ideal (a) and distorted (b) cubic structures of $CaTiO_3$.

3 Results and discussion

3.1 Band structure

The calculated band structure for cubic perovskite $CaTiO_3$ in the high symmetry directions in the Brillouin zone is shown in Figure 1. The energy scale is in eV and the origin of energy was arbitrarily set to be at the valence band (VB) maximum. The bottom most band at -22.3 eV is derived from Ca $3p$ orbitals. The bands at around -17 eV originate from O $2s$ orbitals. Nine valence bands near Fermi level between 0.0 and -5 eV are derived from O $2p$ orbitals. It is clear that the band gap appears between the top-most valence band at R-point and the bottom-most conduction band (CB) at Γ-point. Our band structure agrees well with the band structure obtained by King-Smith and Vanderbilt [14] using first principles ultra-soft-pseudopotential calculations within LDA for $CaTiO_3$. The band structures calculated using TB-LMTO-ASA for $SrTiO_3$ [45] and $BaTiO_3$ [46] are also in good agreement with the ultra-soft-pseudopotential calculation of King-Smith and Vanderbilt [14]. It is to be noted that in the case of $BaTiO_3$ the Ba $5p$ state and in $SrTiO_3$ the Sr $4p$ state appear at higher energy than O $2s$ state whereas in the case of $CaTiO_3$ the O $2s$ state appears at higher energy than Ca $3p$ state. Our calculated value of the indirect band gap for $CaTiO_3$ is ~ 1.5 eV which is lower than the experimentally reported value of 3.5 eV for $CaTiO_3$ [41]. The origin of this discrepancy may be the LDA which underestimates the band gaps even for insulators because of the discontinuity in the exchange-correlation potential which is not taken into account here. Mo *et al.* [50] have calculated the band structure of $SrTiO_3$ and got an indirect (R-Γ) gap ~ 1.45 eV which is about half of the experimental value of 3.2 eV. Kimura *et al.* [34] has also calculated the band structure of the surface of $SrTiO_3$ and obtained an indirect gap ~ 1.79 eV between the R and Γ point.

In the CB region the triplet at 1.5 eV is due to Ti $3d$ t_{2g} band while the singlet at 2.8 eV and doublet at 2.9 eV arise from Ca $4s$ and Ca $3d$ e_g states respectively. Ti $3d$ e_g (doublet) band is located at 4.7 eV. Upper two triplet bands at 6 eV and 8.6 eV are due to Ca $3d$ t_{2g} and Ti $4p$ states respectively. It is to be noted that the Ca $3d$ state in $CaTiO_3$ overlaps with Ti $3d$ state in the conduction band region, whereas the Ba $5d$ state in $BaTiO_3$ [46] and Sr $4d$ state in $SrTiO_3$ [45] appear at higher energy than Ti $3d$ state. We have also calculated the band structure of $CaTiO_3$ considering a small distortion from the ideal cubic structure arising from the tilting of TiO_6 octahedra by an amount 2° and shown in Figure 2. The nature of the band structure qualitatively and quantitatively remains the same, particularly near the Fermi level.

3.2 Density of states

The calculated total DOS and PDOS for ideal cubic $CaTiO_3$ along with experimental results (X-ray photoemission spectroscopy (XPS) spectrum) [42], are shown in Figure 3. In the VB region band A is exclusively composed of O $2p$ orbitals showing the non-bonding state at the top of the valence band. In the lower part of the VB, bands B and C arise due to the contribution of O $2p$ along with Ti $3d$, indicating the formation of p-$d\pi$ and p-$d\sigma$ bonding states respectively. The antibonding combination of these states are the origin of X and Y bands in the CB region

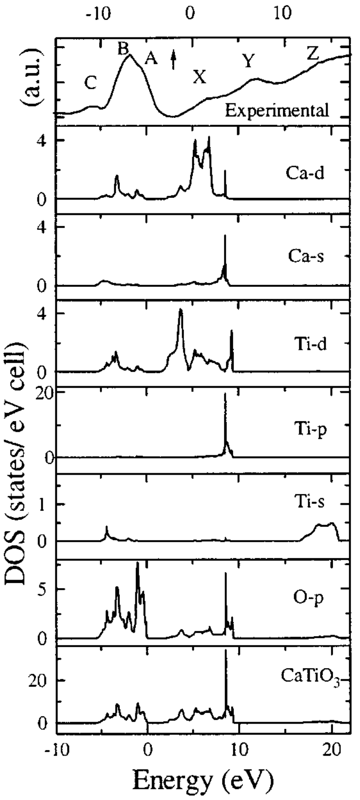

Fig. 3. The calculated DOS and PDOS curves of $CaTiO_3$ is compared with the XPS spectrum (Ref. [42]). The origin of the energy in the calculated spectra is set at the valence band maximum.

respectively. Band X also includes Ca 4*s* and 3*d* orbitals and band Y includes Ti 4*p* orbital. Band Z at higher energy region in the conduction band can be attributed to the Ti 4*s* orbital. In Figure 4 the DOS for distorted cubic $CaTiO_3$ is compared with the ideal cubic structure. In the distorted structure, the DOS in the VB region is almost unchanged. The major quantitative difference is in the CB region.

3.3 Chemical bonding

To have a clear picture about the nature of chemical bonding between the constituent of $CaTiO_3$ we have shown the distribution of charge density in two different planes in Figures 5 and 6. Figure 5 shows a sharing of charge between Ti and O due to Ti 3*d* and O 2*p* hybridization. The spherical distribution of charge around Ca site as shown in Figure 6 indicates that the bonding between Ca with TiO_3 is mainly ionic. It is to be mentioned here that if we consider the self-consistently calculated valence charges within different atomic spheres, the chemical formula for the system may be written as $Ca^{-1.34}Ti^{+1.15}O_3^{+0.06}$. Thus we find a significant deviation from the charge distribution of a prototypical ionic crystal $A^{+2}B^{+4}O_3^{-2}$. Due to the strong hybridization between the O 2*p* and the Ti 3*d* states, there is a large amount of valence charge transfer back to Ti, revealing that the static ionic charge is significantly less than +4 and the O ion is more or less neutral, rather than charged by −2. The amount of extra valence charge of −1.34 for Ca ion is surprising and in contradiction with the traditional picture of simple metals. But, our results agree well with those of Newmann *et al.* for $KNbO_3$ and $KTaO_3$ [51]. Similar nature of bonding in $BaTiO_3$ have been obtained by Cohen and coworkers [9,11] using FLAPW method. In their calculations the Ba ionic charge was kept as +2 and the charges of Ti and O were varied to get the charge neutrality. In the best-fit configuration, O and Ti have charges −1.63 and +2.89 respectively. It must be mentioned that the definition of the charge associated with an atom is different in the TB-LMTO-ASA and the FLAPW. In the former, the charge is that contained in the atomic sphere while in the latter, it is that in the smaller touching spheres. It is therefore not surprising that our results compare well with Neumann *et al.* than Cohen *et al.*. The method of fixing Ba ionic charge at +2 and varying only the Ti and O charges is also very different from the self-consistent procedure in TB-LMTO.

3.4 Optical properties

The interband optical functions such as $\epsilon'(\omega)$, $\epsilon''(\omega)$, $n(\omega)$ and $k(\omega)$ are calculated and shown in Figures 7 and 8. In Figure 7 we have compared our calculated $\epsilon'(\omega)$ and $\epsilon''(\omega)$ spectra with experimental data [41] whereas in Figure 8 a comparison of the calculated and experimental values of $n(\omega)$ and $k(\omega)$ are made. The calculated values agree well with the experimental data for the peak structure in $\epsilon''(\omega)$ curve (Fig. 7b). The first peak in $\epsilon''(\omega)$ curve (Fig. 7b) at 4.5 eV originates from the following transitions: O 2*p* (at 0 eV) → Ti 3*d* t_{2g} (at 4.5 eV) at R-point and O 2*p* (at −0.55 eV) → Ti 3*d* t_{2g} (at 3.9 eV) at X-point. The second peak at 6.3 eV arises from the transition O 2*p* (at −1.3 eV) → Ca 4*s* (at 5 eV) at M-point. The third peak at 6.8 eV comes from the transition O 2*p* (at −0.4 eV) → Ca 3*d* e_g (at 6.5 eV) at M-point. The fourth peak at 8.9 eV arises due to the transitions: O 2*p* (at −4.4 eV) → Ti 3*d* t_{2g} (at 4.5 eV) at R-point and O 2*p* (at −4.3 eV) → Ca 3*d* e_g (at 4.6 eV) X-point. The fifth peak at 9.7 eV may be due to following transitions: O 2*p* (at −3.3 eV) → Ca 3*d* t_{2g} (at 6.4 eV) at R-point, O 2*p* (at −2.6 eV) → Ca 3*d* t_{2g} and e_g (at 7.1 eV) at X-point, O 2*p* (at −4.3 eV) → Ca 3*d* t_{2g} and Ti 3*d* e_g (at 5.35 eV) at X-point, O 2*p* (at −0.35 eV) → Ti 4*p* (at 9.37 eV) at M-point, O 2*p* (at −1.0 eV) → Ti 4*p* (at 8.6 eV) at M-point, O 2*p* (at −1.3 eV) → Ca 3*d* t_{2g} and Ti 3*d* e_g (at 8.3 eV) at M-point. The sixth peak at 11.8 eV originates from the following transitions: O 2*p* (at −3.3 eV) → Ca 3*d* t_{2g} and Ti 4*p* (at 8.5 eV) at R-point, O 2*p* (at −3.2 eV) → Ti 4*p* (at 8.6 eV) at X-point, O 2*p* (at −3.5 eV) → Ca t_{2g} and Ti e_g (at 8.3 eV) at M-point, O 2*p* (at −5.7 eV) → Ti 3*d* e_g (at 6.04 eV) at M-point. The peak at higher energy ($\sim$ 20 eV) may arise due to the transitions from deep lying states such as O 2*s* to Ca and Ti 3*d* states at R- and X-points. These also explain the origin of the peak structures in the the refractive index $n(\omega)$ (Fig. 8a) and extinction coefficient

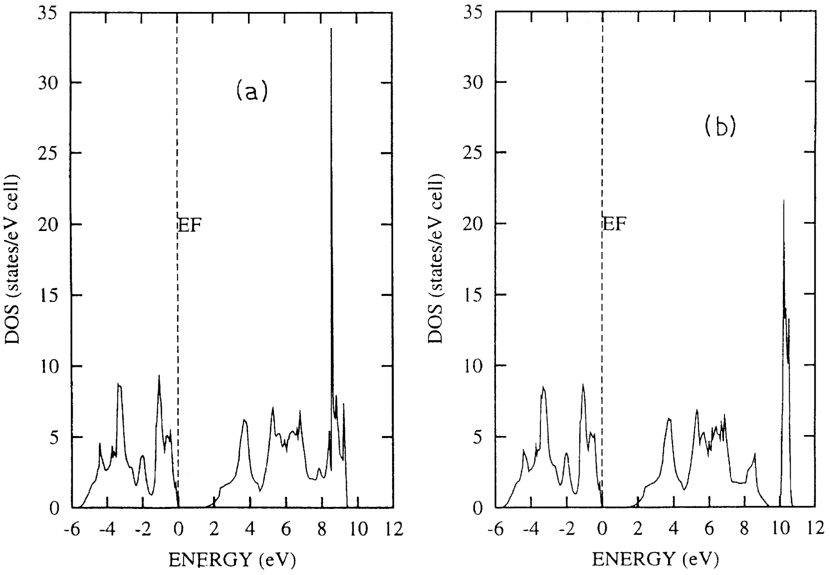

Fig. 4. A comparison of DOS for ideal (a) and distorted (b) cubic structures of CaTiO$_3$ near Fermi level.

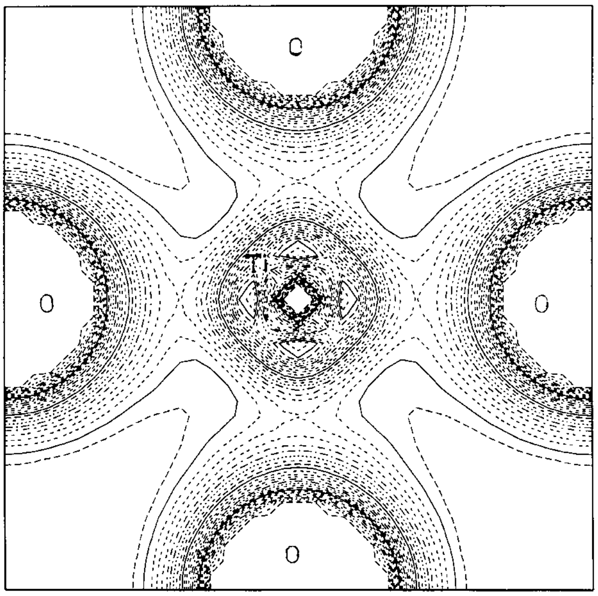

Fig. 5. The valence charge density contour in the (200) plane for CaTiO$_3$.

$k(\omega)$ (Fig. 8b) spectra. Overall, our theoretical spectra are found to be in good agreement with experiments for lower energy range. At higher energy the theoretical value do not follow the experimental trend. This discrepancy may be due to the inadequacy of the LDA to reproduce the band gap and the higher energy excited states properly. Corrections like the "scissors operator" technique corrects these discrepancies somewhat. The effective number of valence electrons per unit cell contributing in the interband transitions can be calculated by means of the sum rule

$$n_{\mathrm{eff}}(E_{\mathrm{m}}) = \frac{2m}{Ne^2h^2} \int_0^{E_m} E\, \epsilon''(E)\, \mathrm{d}E$$

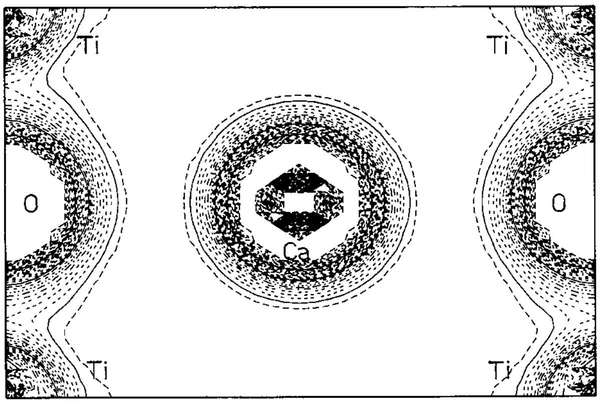

Fig. 6. The valence charge density contour in the (110) plane for CaTiO$_3$.

where E_{m} denotes the upper limit of integration. The quantities m and e are the electron mass and charge respectively. N stands for the electron density. The results are shown in Figure 9. The $n_{\mathrm{eff}}(E_{\mathrm{m}})$ reaches a saturation value above 25 eV. This shows that the deep-lying valence orbitals do not participate in the interband transition.

4 Conclusions

We have made a detailed investigation of the electronic structure and optical properties of perovskite CaTiO$_3$ using the TB-LMTO method. The total DOS obtained from our first principles calculations are compared with experimental results [42]. The origin of the various experimentally observed bands have been explained. It has been concluded that the top of the VB is mainly composed

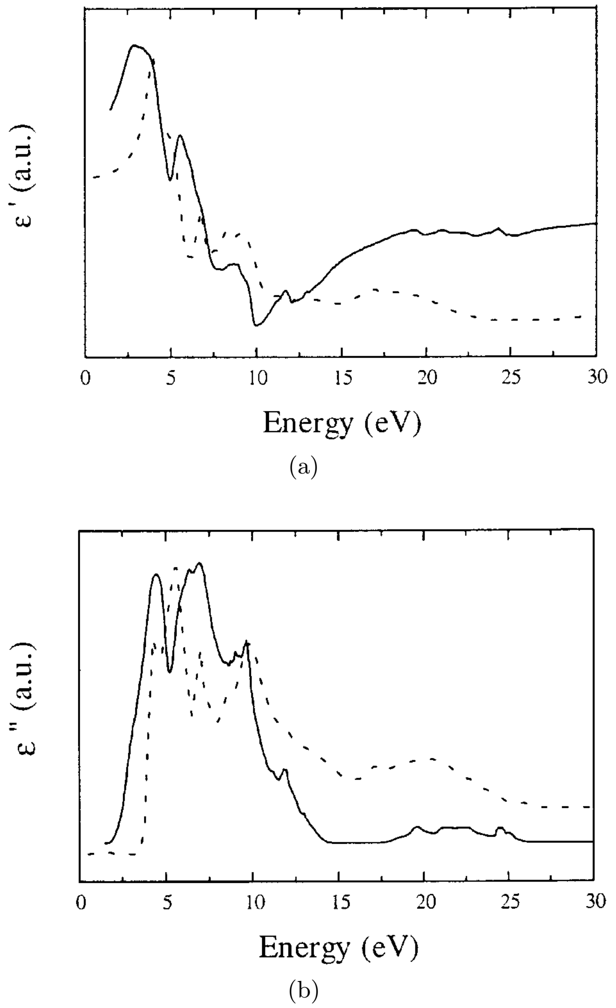

(a)

(b)

Fig. 7. The calculated (a) real ($\epsilon'(\omega)$) and (b) imaginary ($\epsilon''(\omega)$) parts of complex dielectric constant of $CaTiO_3$ are compared with the experimental data (Ref. [41]): dotted line - experimental, continuous line - theoretical.

of the O $2p$ orbitals in non-bonding states and the lower part of the VB is formed by bonding states between the Ti $3d$ and O $2p$ orbitals. The CB mainly consists of $3d$, $4s$ and $4p$ states of Ti and $3d$ and $4s$ states of Ca. The calculations show that the fundamental gap of $CaTiO_3$ is indirect. Our calculated fundamental gap of 1.5 eV is smaller than the experimentally reported value of 3.5 eV [41]. Using the site and angular momentum projected DOS and band structure we have analyzed the interband contribution to the optical properties. The chemical bonding of $CaTiO_3$ is also analyzed. The TiO_3 complex is bonded covalently while the Ca and TiO_3 constituents are bonded mainly ionically. We have examined the energy dependent dielectric constants as well as related quantities such as refractive index and extinction coefficient and compared with the experimental results [41] for $CaTiO_3$. The calculated results show a very good agreement with the experimental data. Lastly, the effective number of electrons per unit cell participating in the interband transitions are calculated.

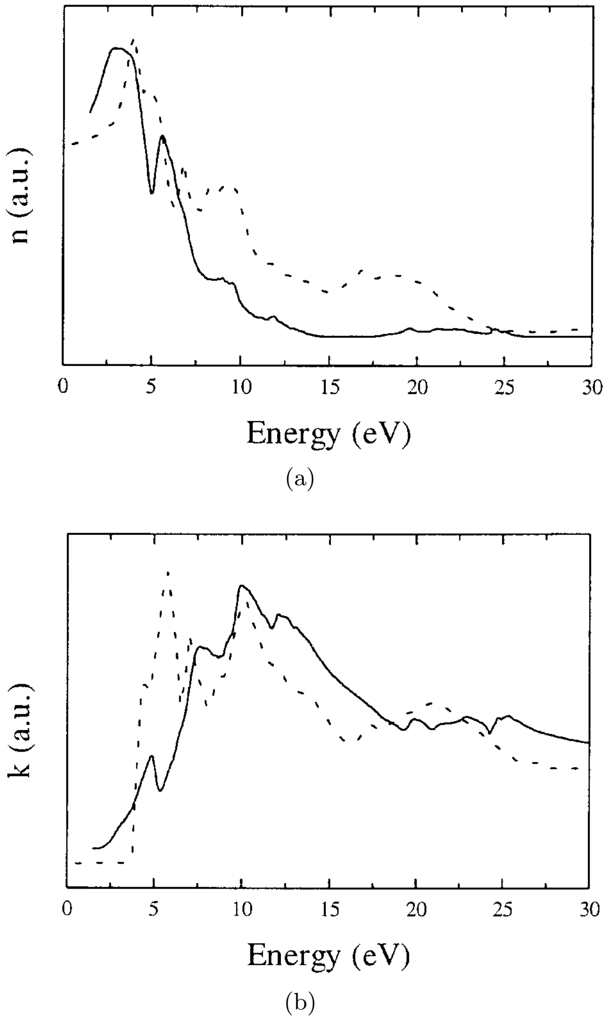

(a)

(b)

Fig. 8. The calculated (a) the refractive index $n(\omega)$ and (b) the extinction coefficient $k(\omega)$ of $CaTiO_3$ are compared with the experimental results (Ref. [41]): dotted line - experimental, continuous line - theoretical.

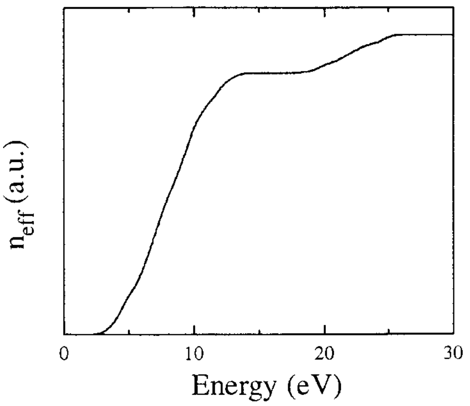

Fig. 9. The calculated effective number of electrons (n_{eff}) participating in the interband optical transitions of $CaTiO_3$.

References

1. M.E. Lines, A.M. Glass, *Principles and Applications of Ferroelectrics and Related Materials* (Clarendon, Oxford, 1977).
2. R. Viana, P. Lunkenheimer, J. Hemberger, R. Böhmer, A. Loidl, Phys. Rev. B **50**, 601 (1994).
3. K.A. Müller, H. Burkard, Phys. Rev. B **19**, 3593 (1979).
4. B.J. Kennedy, C.H. Howard, B.C. Chakoumakos, J. Phys. Cond. Matt. **11**, 1479 (1999).
5. S. Sasaki, C.T. Prewitt, J.D. Bass, Acta Crystallogr. C **43**, 1668 (1987).
6. R.H. Buttner, E.N. Maslen, Acta Crystallogr. B **48**, 644 (1992).
7. K.H. Wyrich, R. Siems, Z. Phys. B **61**, 63 (1985).
8. K.H. Wyrich, R.P. Madenach, Ferroelectrics **111**, 9 (1990).
9. R.E. Cohen, H. Krakauer, Phys. Rev. B **42**, 6416 (1990).
10. R.E. Cohen, H. Krakauer, Ferroelectrics **136**, 65 (1992).
11. R.E. Cohen, Nature **358**, 136 (1992).
12. D.J. Singh, L.L. Boyer, Ferroelectrics **136**, 95 (1992).
13. R.D. King-Smith, D. Vanderbilt, Ferroelectrics **136**, 85 (1992).
14. R.D. King-Smith, D. Vanderbilt, Phys. Rev. B **49**, 5828 (1994).
15. R.D. King-Smith, D. Vanderbilt, Phys. Rev. B **47**, 1651 (1993).
16. D. Vanderbilt, R.D. King-Smith, Phys. Rev. B **48**, 4442 (1993).
17. W. Zhong, R.D. King-Smith, D. Vanderbilt, Phys. Rev. Lett. **72**, 3618 (1994).
18. Ph. Ghosez, X. Gonze, J.-P. Michenaud, Europhys. Lett. **33**, 713 (1996).
19. Ph. Ghosez, X. Gonze, J.-P. Michenaud, Ferroelectrics **153**, 91 (1994).
20. C. Lee, Ph. Ghosez, X. Gonze, Phys. Rev. B **50**, 13379 (1994).
21. Ph. Ghosez, X. Gonze, J.-P. Michenaud, Ferroelectrics **164**, 113 (1995).
22. Ph. Ghosez, X. Gonze, Ph. Lambin, J.-P. Michenaud, Phys. Rev. B **51**, 6765 (1995).
23. A.V. Postnikov, T. Neumann, G. Borstel, M. Methfessel, Phys. Rev. B **48**, 5910 (1993).
24. A.V. Postnikov, T. Neumann, G. Borstel, Phys. Rev. B **50**, 758 (1994).
25. W. Zhong, D. Vanderbilt, K.M. Rabe, Phys. Rev. Lett. **73**, 1861 (1994).
26. W. Zhong, D. Vanderbilt, K.M. Rabe, Phys. Rev. B **52**, 6301 (1995).
27. D. Vanderbilt, Phys. Rev. B **41**, 7892 (1990).
28. W. Zhong, D. Vanderbilt, Phys. Rev. Lett. **74**, 2587 (1995).
29. W. Zhong, D. Vanderbilt, Phys. Rev. B **53**, 5047 (1996).
30. J. Padilla, W. Zhong, D. Vanderbilt, Phys. Rev. B **53**, R5969 (1996).
31. A. Garcia, D. Vanderbilt, Phys. Rev. B **54**, 3817 (1996).
32. R.E. Cohen, J. Phys. Chem. Solids **57**, 1393 (1996).
33. J. Padilla, D. Vanderbilt, Phys. Rev. B **56**, 1625 (1997).
34. S. Kimura, J. Yamauchi, M. Tsukada, S. Watanabe, Phys. Rev. B **51**, 11049 (1995).
35. Z.Q. Li, J.L. Zhu, C.Q. Wu, Z. Tang, Y. Kawazoe, Phys. Rev. B **58**, 8075 (1998).
36. M. Cardona, Phys. Rev. **140**, A651 (1965).
37. F.M. Michel-Calendini, G. Mesnard, J. Phys. C. Solid State Phys. **6**, 1709 (1973).
38. D. Bäuerle, W. Braun, V. Saile, G. Sprüssel, E.E. Koch, Z. Phys. B **29**, 179 (1978).
39. F.M. Michel-Calendini, H. Chermette, J. Webers, J. Phys. C. Solid State Phys. **13**, 1427 (1980).
40. D. Bagayoko, G.L. Zhao, J.D. Fan, J.T. Wang, J. Phys. Cond. Matt. **10**, 5645 (1998).
41. K. Ueda, H. Yanagi, H. Hosono, H. Kawazoe, J. Phys. Cond. Matt. **10**, 3669 (1998).
42. K. Ueda, H. Yanagi, H. Hosono, H. Kawazoe, J. Phys. Cond. Matt. **11**, 3535 (1999).
43. O.K. Andersen, O. Jepsen, Phys. Rev. Lett. **53**, 2571 (1984).
44. W. Kohn, L.J. Sham, Phys. Rev. **140**, A1133 (1965).
45. S. Saha, T.P. Sinha, A. Mookerjee, J. Phys. Cond. Matt. **12**, 3325 (2000).
46. S. Saha, T.P. Sinha, A. Mookerjee, Phys. Rev. B **62**, 8828 (2000).
47. U. von Barth, L. Hedin, J. Phys. C. Solid State Phys. **5**, 1629 (1972).
48. O. Jepsen, O.K. Andersen, Solid State Commun. **9**, 1763 (1971).
49. P. Ravindran, A. Delin, B. Johansson, O. Eriksson, Phys. Rev. B **59**, 1776 (1999).
50. S.D. Mo, W.Y. Ching, M.F. Chisholm, G. Duscher, Phys. Rev. B **60**, 2416 (1999).
51. T. Neumann, G. Borstel, C. Scharfschwerdt, M. Neumann, Phys. Rev. B **46**, 10623 (1992).